Microfluidic Biosensor for the In Vitro Electrophysiological Characterization of Actin Bundles

Jorge Manrique Castro, Nilab Azim, Nicholas Castaneda, Ellen Kang, and Swaminathan Rajaraman, *Member, IEEE*

***Abstract*— The essential cytoskeletal protein actin and its functions are paramount for motility, communication, and locomotive processes in eukaryotic cells. Detection and quantification of actin protein is of great interest for *in vitro* studies potentially elucidating unknown cellular mechanisms affecting drug responses with an extension to the study of disease states (e.g., study of neurodegenerative disorders). To this end, development of biomedical platforms and biosensors plays an important role in providing reliable and sensitive devices to study such intracellular constructs. Here, we present for the first time the microfabrication, characterization, testing, and electrical/interfacial modeling of a microfluidic biosensor for actin protein characterization. The device allows for the interaction and characterization of actin bundles using electrochemical impedance spectroscopy (EIS). The device was tested with 1 μM and 8 μM actin bundles concentrations producing shifts in impedance response in the significant biological frequency of 1 kHz from 17 to 30 kOhm (kΩ). Interfacial capacitance and electrical modeling showed that at increasing actin bundles concentrations, the distance from the electrode to the diffusion region (Debye length) was reduced from 386 to 136, and from 1526 to 539 Å. Interfacial capacitance was evaluated for 1 μM concentration at two dielectric constants ($\varepsilon_r = 5$ and 78) resulting in 3.8 and 15.6 mF/m^2 respectively. Similarly, for 8 μM concentration, interfacial capacitance resulted in 10.1 and 43.3 mF/m^2 for the same values of ε_r. Based on these theoretical calculations, the interface model could accurately predict the quantification of the actin bundles previously elucidated by the experimental EIS method. [2023-0180]**

***Index Terms*— Actin, electrochemical impedance spectroscopy (EIS), interdigitated electrodes (IDE), interfacial capacitance, microfluidic biosensor, interface modeling.**

I. Introduction

ACTIN is the essential protein residing in the cytoskeletal network of eukaryotic cells, and is responsible for important biological functions such as cell motility [1], [2], organelle transport, phagocytosis, and cell division [3]. Its base structure, i.e., actin monomers (G-actin), can polymerize to form double-helical actin filaments (F-actin, linear biopolymers that behave as charged polyelectrolytes [4]. In controlled microenvironments, F-actin, can be exposed to biochemical factors like macromolecular crowding [5], [6], [7] and electrostatic interactions [8], and these interactions can result in the formation of actin bundles [9], [10], [11]. Mechanical and structural properties of actin bundles are modulated by these biochemical processes as well as by the network connectivity [10], [12], [13].

The organization of F-actin into higher ordered bundles provides cells with mechanical integrity and structural support. Numerous actin-binding proteins (ABPs) modulate actin architectures and functions in cells by tightly controlling actin assembly dynamics and mechanics [2], [14]. Considering that actin filaments potentially can serve as electric transmitter by conducting ionic currents [15], actin filament and bundles assembly/disassembly dynamics and mechanics may play a central role in cellular electrophysiology. However, it is unknown how electric stimuli modulate the mechanical properties of actin bundles, and vice versa.

Although it has been hypothesized that actin filaments may play the role of an electrical transmitter, currently very little work has been reported on the interfacing of actin with electrical stimuli other than theoretical modeling [16]. In order to develop and study responses of actin to various electrical stimuli, an optimized development of biomedical sensor platforms is needed. Currently, there are several microfabrication techniques and characterization methods to produce quantitative and qualitative information from biological entities such

Manuscript received 3 October 2023; revised 18 February 2024; accepted 7 March 2024. Date of publication 25 March 2024; date of current version 4 June 2024. The work of Nicholas Castaneda and Ellen Kang was supported by the National Science Foundation under Grant 1943266. The work of Jorge Manrique Castro, Nilab Azim, and Swaminathan Rajaraman was supported in part by the UCF Start-Up Funding and in part by Florida High Tech Corridor Matching Funds. Subject Editor K. Cheung. *(Corresponding author: Jorge Manrique Castro.)*

Jorge Manrique Castro is with the NanoScience Technology Center, University of Central Florida, Orlando, FL 32816 USA (e-mail: jorge.manrique.castro@ucf.edu).

Nilab Azim was with the NanoScience Technology Center and the Department of Chemistry, University of Central Florida, Orlando, FL 32816 USA. She is now with the National Aeronautics and Space Administration (NASA), Merritt Island, FL 32953 USA (e-mail: nilab.azim@nasa.gov).

Nicholas Castaneda is with the NanoScience Technology Center and the Burnett School of Biomedical Sciences, University of Central Florida, Orlando, FL 32826 USA (e-mail: nicholas.castaneda27@gmail.com).

Ellen Kang is with the NanoScience Technology Center, the Department of Physics, and the Department of Materials Science and Engineering, University of Central Florida, Orlando, FL 32826 USA (e-mail: ellen.kang@ucf.edu).

Swaminathan Rajaraman is with the NanoScience Technology Center, the Department of Materials Science and Engineering, the Department of Electrical and Computer Engineering, and the Burnett School of Biomedical Sciences, University of Central Florida, Orlando, FL 32816 USA (e-mail: swaminathan.rajaraman@ucf.edu).

This article has supplementary material provided by the authors and color versions of one or more figures available at https://doi.org/10.1109/JMEMS.2024.3376238.

Digital Object Identifier 10.1109/JMEMS.2024.3376238

as the well-known COVID-19 virus [17], [18], [19], [20], electrogenic cells [21], [22], [23], and bacteria [24], [25]. Among these, 2D and 3D microelectrode arrays (MEAs) [26], interdigitated electrodes (IDE) [27], microfluidics [28], and electrical biosensors [29] are well characterized with established microfabrication processes [30], [31], [32] and electrochemical principles [33]. Our group, previously explored the development of IDE-based BioMEMS platforms optimizing electrode geometry, spacing and substrate nanostructure to enhance sensitivity and multi-modality of the platform (Electrochemical Impedance Spectroscopy + Surface Plasmon Resonance) [34]. Smaller electrode gaps and increased surface area were found to be ideal in order to improve device sensitivity in a tailored fashion.

Microfluidic systems are suitable structures to run samples for biochemistry and biomechanical studies of actin protein as reported in [35]. In order to operate reagents with a suitable pressure, flow velocity and gain control over actin dynamics along the microchannel, structures with dimensions of hundreds of microns wide and tens of microns high are desired [36].

There is also a great interest in developing technologies for intra-cellular measurements in real-time and gain an understanding of the evolution of cellular physiology *in vivo* [37]. However, the *in vitro* study of intra-cellular proteins such as actin would elucidate information about the underlying physics and would ease procurement of electrical signal transductions emanating from the response of actin to various agents in a controlled setting. The interest of research in actin protein arises from the fact that experimental studies do not correspond quantitatively with predictive models [38]. Actin filaments are usually the focus of investigation and electrical modeling for actin bundles is lacking. Expanding the research to higher-order structures such as bundles would also provide insights about the conductive behavior of protein networks with mechano-electrical signaling characteristics [39]. However, biomedical platforms specifically designed for studies of actin bioprotein are still lagging.

Herein, we propose for ***the first time to our knowledge*** a simple, easy-to-use, and effective solution to quantify the electrophysiological properties of actin bundles based on IDEs integrated within microfluidic channels, i.e., microfluidic biosensor for the collection of impedance data from EIS upon actin injection at various concentrations. The fabricated device will take advantage of techniques for rapid prototyping such as soft-lithography [40] and laser micromachining [41], allowing for rapid prototyping modifications, and easy integration of subcomponents as illustrated in the microfabrication process flow depicted in the schematic in **Fig. 1**. Laser micromachining advantages such as high precision and quality for complex designs are ideal for biomedical applications [42]. There is also a financial point of view that makes laser micromachining attractive when compared to cleanroom processes (e.g., photolithography). Time spent in producing prototypes, specialized training, high cost of mask aligners and photolithographic tools, and chemical handling are some of the cons that are overcome by this technology when compared to a cleanroom setting [43]. Even with the right selection of the laser and optical system, the attained resolution is comparable to its photolithographic counterpart [44]. In addition to the microfabrication process of the microfluidic biosensor, electrical and interface capacitance modeling is proposed to be explored to correlate actin protein interactions with the IDE with proposed theoretical ideas.

II. Materials and Methods

A. Design (IDE and Microchannel)

IDE and microchannel were designed using (Computer-Aided Design) CAD software (Solidworks, Dassault Systèmes). IDE is composed of two electrodes, 20 fingers each with 1 mm length, 200 μm width, and a gap (i.e., pitch) of 25 μm between them. Two squared contact pads of 5 mm per side are included in the design to measure in-line impedance.

The microchannel is designed to sit atop the IDE measured 10 mm (length) by 150 μm (width). Microchannel inlet and outlet ports are 1.5 mm diameter each. Both designs were exported to the multimodal laser system (QuikLaze 50ST2, New Wave Research Inc.) software, for machining the design into the respective materials as discussed in following subsections.

B. IDE Microfabrication

Kapton® film (2 mil thickness) was used to create a stencil mask and subsequently a gold (Au) deposition process on a glass slide was performed as presented in optical micrographs (**Fig. 2a-c**). As observed in **Fig. 2b**, the affixing process of the Kapton mask onto the glass substrate produced gaps on the stencil-glass interface impacting the edges of the IDE upon metallization (see **Fig. 2d**. inset). This lack of intimate contact caused a shadow masking effect along the borders. It is important to mention that edges are not relevant to the device reliability or actin interfacing effects as they are not in contact with the microfluidic system or biological sample. The metallization process was performed using a sputtering system for 300 sec at a rate of 15 nm/min (EMS150T ES, Quorum Technologies).

Kapton® stencil mask was ablated using the IR laser source (1064 nm) from the multimodal laser micromachining system with 90% power, 50 Hz frequency, scan speed 50 μm/sec, and two passes. After Au metallization, fingers on the IDE were ablated using green light laser source (532 nm) set to 50% power, 50 Hz frequency, scan speed 70 μm/sec, and one pass (**Fig. 2d**).

Precise alignment is required for the ablation of the fingers on the IDE. In order to facilitate this, a supporting white sheet of paper with alignment marks kept below the glass slide was used to match the fingers design on the IDE prior to laser ablation.

C. Microchannel Microfabrication

Template molding technique was carried out using Kapton® tape (2 mil thickness) onto a petri dish acting as the template and PDMS micromolding atop this template. To create the microchannel template mold, the Kapton® sheet was laser

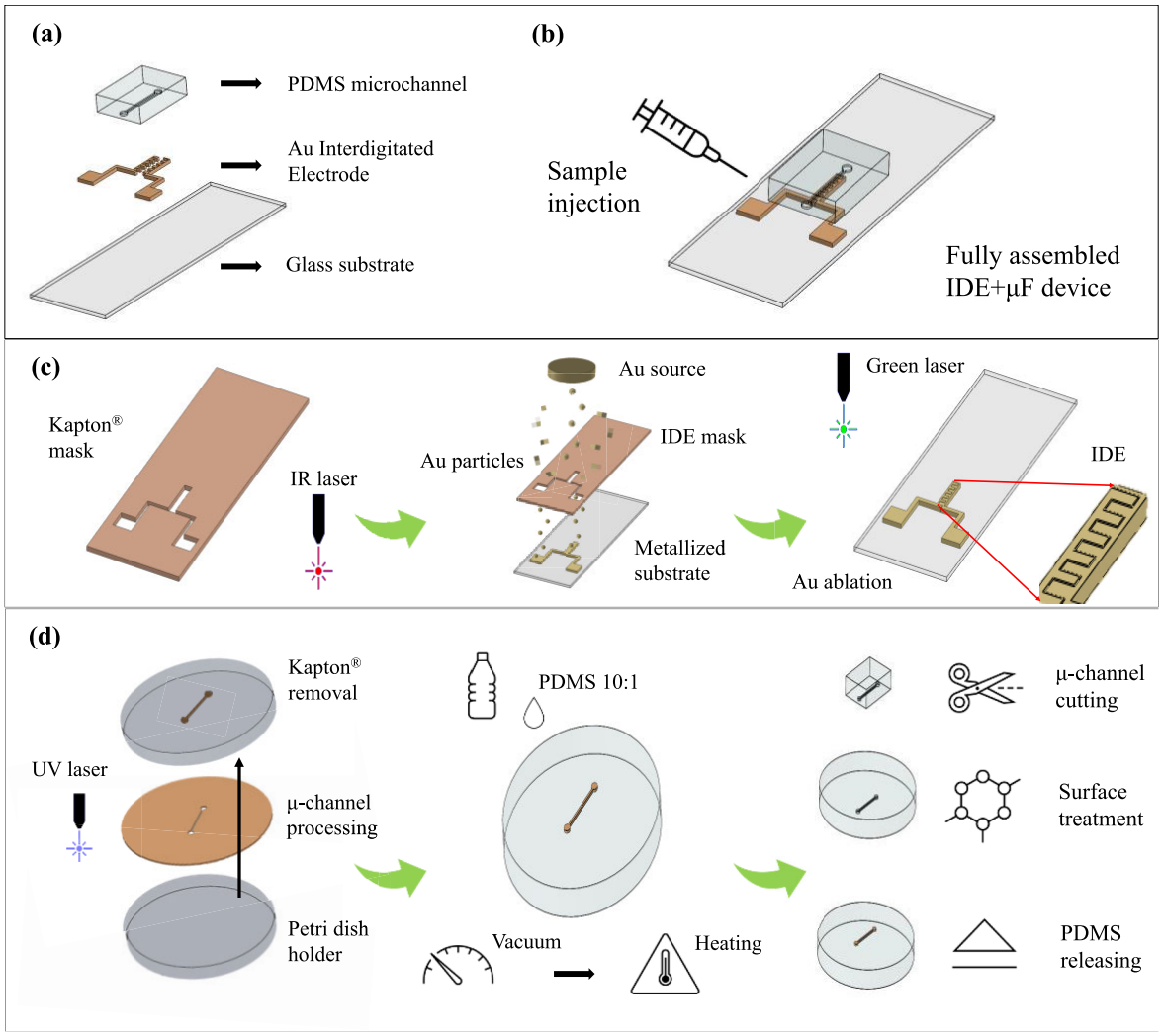

Fig. 1. Schematic of the fabrication process for the IDE-based actin microfluidic chip sensor. (a) Left: Exploded device detailing microchannel, gold metallized interdigitated electrode (IDE) and glass substrate. Right: Assembled actin detection platform with inlet and outlet ports for sample injection and exposed contact pads for electrochemical impedance spectroscopy (EIS) measurements. (c) IDE microfabrication process. Kapton® mask is laser micromachined to be further used during the metallization process. Gold is sputtered onto the glass substrate at vacuum level. Gold ablation is performed with multimodal laser to isolate electrodes generating the IDE with minimum gap. (d) PDMS microchannel microfabrication process. Kapton® tape is attached to the bottom of a petri dish and laser cut in order to left the positive feature of the microchannel on the bottom. PDMS mix is poured into the petri dish to start the molding process. Sample is put in vacuum to remove any air inside the mix. After heating, the PDMS mold is ready to be released from the petri dish holder. Plasma surface treatment is performed in the microchannel surface to enhance bonding energies to glass. Lastly, mold is cut to the desired size and is ready for the final assembly.

cut with UV light source (355 nm) at 50% power, 50 Hz frequency, 50 μm/sec scan speed, and 2 passes (**Fig. 3a-b**).

PDMS solution was created using the standard ratio of 10:1 (18.2 g: 1.8 g; Base elastomer: Curing agent) and mixed for 2 min, and poured into the petri dish. PDMS solution was degassed using a bell jar vacuum system (0.8 bar) in order to evacuate any air bubbles. Lastly, PDMS is cured at 60 °C for 4 hr. and the micromolded channel was released from the petri dish as depicted in **Fig. 3c**.

D. Device Assembly

A released PDMS mold and Au metallized glass slide are placed into an oxygen plasma chamber (Plasma Etch Inc.) and treated for 20 sec prior to bonding the substrates together. PDMS mold and isolated IDE structure were carefully aligned (stereoscope) by placing the microfluidic channel structure onto the central and longitudinal region of the IDE as observed in **Fig. S1** (Top View). Additional improvement on the bonding process was carried out by thermally annealing the assembled biosensor in an oven for 1 hr. at 80 °C.

Inlet and outlet ports are created by using a biopsy punch (1 mm width) on the PDMS. Photograph of the actual impedimetric actin biosensor components are detailed in **Fig. S2** in Supplementary Materials.

E. Actin Sample Preparation and TIRF Imaging

Actin purification and sample preparation followed the protocol as described [45], [46]. Actin polymerization was achieved by adding 1/10th volume of 10× KMI buffer (50 mM KCl, 2 mM $MgCl_2$, 10 mM imidazole, pH 7.0, 1 mM ATP, and 1 mM DTT) to achieve 8 μM filament-actin concentration. F-actin were subsequently diluted with the KMI buffer solution

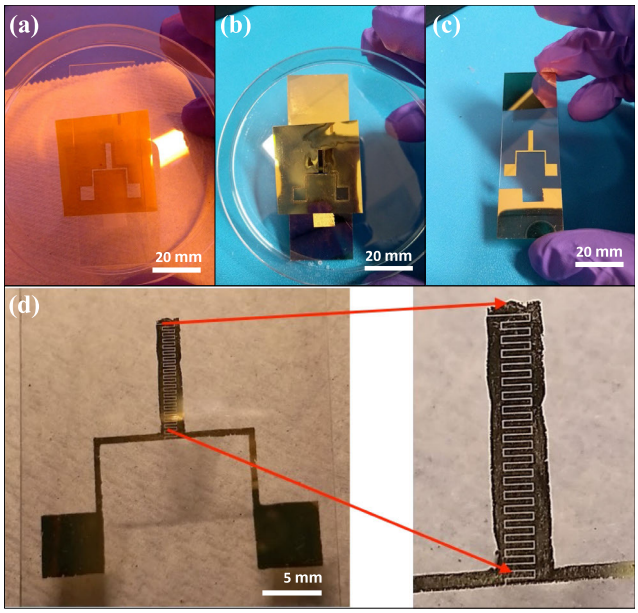

Fig. 2. IDE microfabrication process. (a) Kapton® mask is created by laser ablation using 1064 nm source (IR). (b-c) Gold is sputtered in vacuum onto pre-treated glass slide to generate the non-isolated IDE. (d) Multimodal laser is used with visible light (Green at 532 nm) to ablate gold and isolate electrodes in the IDE as depicted in the zoomed view.

to 1 μM. Actin bundle formation occurred at 8 μM with the addition of MI buffer (30 mM Mg^{2+}, 1 mM ATP, 1 mM DTT, 10 mM imidazole pH 7.0) and subsequently diluted to 1 μM using the MI buffer solution. The low concentration of actin bundles was controlled by its dilution with the MI buffer.

Total Internal Reflection Fluorescence (TIRF) microscopy (Nikon Eclipse Ti) was performed and supported by a Hamamatsu Image EM X2 CCD camera and a 100X oil immersion objective (N.A. 1.49) with a pixel size of 0.16 μm at room temperature (~22 °C) After 1 hr. of filament flow in the microchannel ensuring equilibrium at room temperature, buffer for bundles polymerization was introduced and the solution was diluted. Injection of F-actin and actin bundles into the device was achieved by active flowing with syringes and gentle positive pressure along the microchannel (**Fig. 4**).

F. EIS Characterization

Electrochemical Impedance Spectroscopy (EIS) was performed in-line upon injection of F-actin and actin bundles to the inlet port of the microfluidic biosensor at 1 μM and 8 μM concentrations, respectively. An impedance baseline provided by the KMI and MI buffers was also experimentally derived. The two-electrodes system is presented in **Fig. 5**. Frequency was swept from 1 Hz to 10 MHz using a vector network analyzer (Bode 100, Omicron Lab). Bode and Nyquist plots were generated after data processing in Origin 2020b software with 1kHz impedance values highlighted for each actin concentration due to its relevancy in biomedical applications. Electrophysiological measurements were performed in triplicate for each of the buffer, F-actin, and actin bundle concentrations.

G. Modeling (Electrical and Interface)

An electrical model from the impedance spectrum for actin bundles was derived. The electrical model follows the Randles' electrochemical equivalent circuit representation. This model comprises a solution resistance R_S, a charge transfer resistance R_{CT} in-series to a diffusion Warburg element W, and this branch in-parallel to a double layer capacitive element represented by the Constant Phase Element (CPE). Model representation is depicted in **Fig. 6**.

Values for each element are derived through EISSA software and presented here with its interpretation. EISSA stands for Electrochemical Impedance Spectroscopy Spectrum Analyser and was developed by A. Bondarenko and G. Ragoisha [47]. EISSA is a standalone program for analysis and simulation of impedance spectra. The analyzer routine is based on algorithms of potentiodynamic spectrometry. The software is free for noncommercial use and accessible from http://www.abc.chemistry.bsu.by/vi/analyser/.

Interface phenomena (e.g., interfacial capacitance) is also modeled along with exponential potential decay expressed by the Debye length in the electrochemical cell. Capacitive effects due to species diffusion under AC small signal conditions are detailed. Interface capacitance and the Debye length from the space charge layer region are calculated theoretically [48], [49] using actin-related protein parameters such as condensed and diffuse solution layers dielectric constant, and bare, hydrated size of Mg^{2+} ions reported in the literature [16], [50].

III. Results and Discussion

A. Physical Characterization

Design to device comparison of the microfluidic biosensor was performed using laser confocal microscopy and the results are presented in **Fig. 3d-f**. A 3D and 2D representation of the IDE embedded within the microfluidic biosensor is additionally depicted in **Fig. S1**, emphasizing microchannel superposition atop the IDE and its dimensions. Features such as the microchannel and the IDE were evaluated to analyze the accuracy of the microfabrication processes and the tools involved.

1) Laser Confocal Microscopy Characterization: Experimental dimensions on the microchannel and IDE can be compared to the design on the **Table I**. To quantify the reproducibility of the device fabrication, laser cutting error is characterized. It is observed that laser cutting combined with soft lithography with PDMS presented 21% and 17% error respectively during the microfabrication process of the microchannel for the dimensions of the width and the height respectively. It is hypothesized that these errors arise from the laser micromachining on Kapton material for the microchannel mold (error % in width) and PDMS shrinking (error % in height) after the curing step [51]. Laser ablation of the metal (Au) produced an error lower than 10% on the finger's dimensions (length and width).

This error, while acceptable, is due to the ablated area of ~20-30 μm produced by the green light source of the multimodal laser system. The highest error (12%) on laser ablation was measured in the gap (i.e., pitch) generated for the

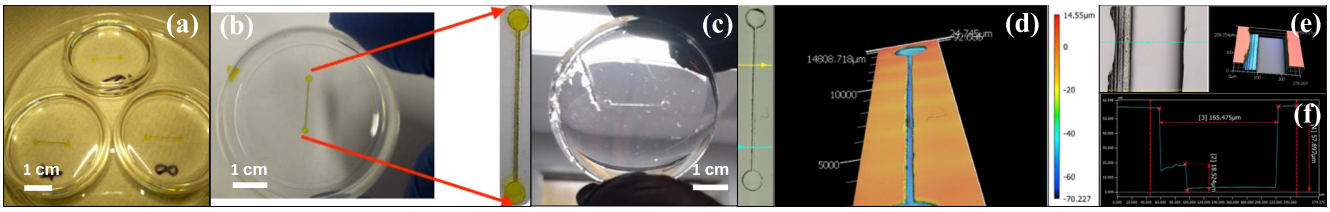

Fig. 3. Microchannel microfabrication process. (a) Petri dish is used as Kapton® tape holder to generate the microchannel pattern on the bottom using UV laser micromachining. (b) Unwanted Kapton® is released from the holder leaving the microchannel pattern only. (c) Soft-lithography technique with PDMS is implemented in a ratio of 10:1 (silicon elastomer and curing agent), and after curing the mold is released from the petri dish. (d-f) Laser confocal microscopy microchannel characterization. 3D profile is obtained along the microchannel, and metrics such as height (∼57 μm) and width (∼167 μm) are evaluated on the microfabrication process.

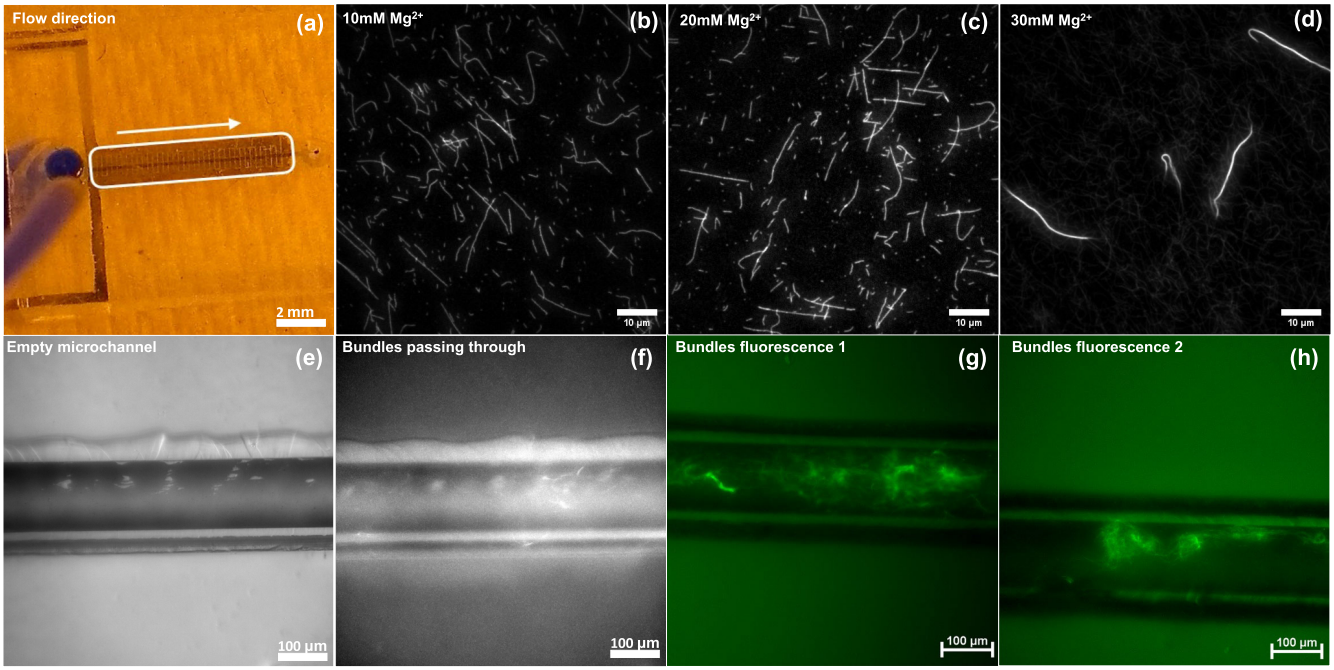

Fig. 4. Actin protein preparation and sample injection. (a) Flow direction represented by the white arrow along the IDE+microfluidic system from inlet to outlet. (b-d) TIRF microscopy imaging of actin bundles formation at different concentrations of Mg^{2+} divalent cation. (e-f) TIRF imaging for comparison of an empty microchannel and filled microchannel with actin bundles protein flowing as the sample. (g-h) TIRF images confirming presence of actin bundles inside the microfluidic chip.

green light source during the metal micromachining process. Differences in these values are referenced to the data delivered by the manufacturer at the same wavelength and energy range, which was set to 25 μm for trimming gold [52].

2) Surface Roughness: Surface roughness of the metallized glass slide was measured in order to identify its relation to the interface phenomena during the impedance measurements. The mean value of this parameter was 7 μm for the Au thin film using a metal sputter coating system (EMS150T ES, Quorum Technologies).

Glass slide was prepared for an enhanced metal deposition using a pre-treatment with an overnight bath of potassium hydroxide (KOH) followed by rinsing in DI water for 30 mins. KOH treatment is an aggressive wet-etching technique of glass resulting in increased roughness of the treated surface when compared to the thickness of the deposited gold layer (∼75 nm) for this work. Visual schematic representation is presented in **Fig. S3**. The surface roughness was obtained in three different areas along the scribed IDE surface, as represented in **Fig. S1** for the central area. Result of this value is additionally showcased on **Table I**.

B. Actin Protein Impedance-Based Characterization

1) Actin Bundles and Filament Spectrum: In-line impedance measurements showed an increased tendency in the formation of the kinetic region in the impedance spectrum upon injection of actin bundles at higher concentrations into the system. Specific values at 1 kHz frequency were recorded and averaged as presented in the Bode plots from **Fig. 7**. It can be observed that the baseline (MI Buffer) showed a value of ∼1 kΩ. Once actin bundles at 1 μM concentration was introduced into the sensor, specific-frequency impedance magnitude increases approximately 20-fold to ∼17 kΩ. Subsequently, an increase of approximately 30-fold for 8 μM actin bundles is registered with values close to ∼30 kΩ.

Furthermore, Nyquist plots depict a clear shifting from the diffusion region (tilted line) to the kinetic region (semi-circle) of the electrochemical cell in all cases: MI buffer,

TABLE I
SURFACE ROUGHNESS AND DEVIATION ON THE MICROFABRICATION PROCESS OF MICROCHANNEL AND IDE FOR THE ACTIN BIOSENSOR

Samples (n)	Feature	Mean Surface Roughness (μm)	Design Dimension (μm)	Device Dimension (μm)	Error (%)	Microfabrication process
3	Au-metallized IDE	7.708	-	-	-	Metal Sputtering
1	IDE Finger (Length)	-	1000	995	0.5	Laser Ablation
1	IDE Finger (Width)	-	200	219	9.5	Laser Ablation
1	IDE Fingers (Gap)	-	25	28	12	Laser Ablation
3	PDMS Microchannel (Width)	-	150	182	21	Laser Cutting + Soft-Lithography
8	PDMS Microchannel (Height)	-	51	60	17	Laser Cutting + Soft-Lithography

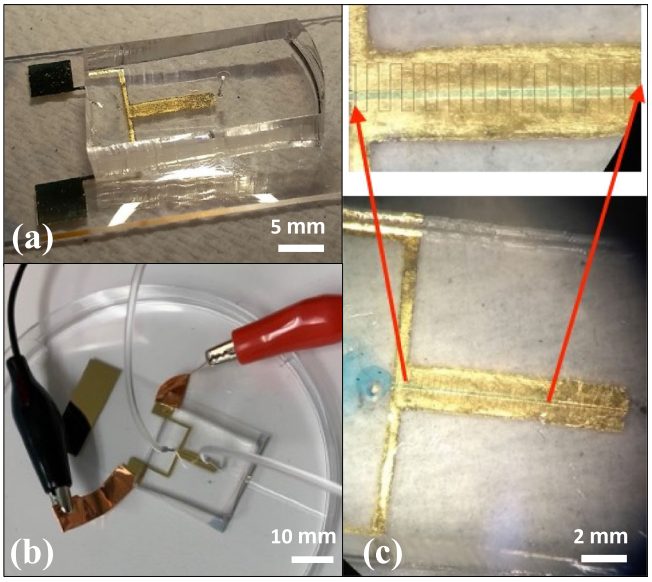

Fig. 5. (a-b) Actual actin sensor platform and electrical characterization. Connection of the system to the vector analyzer for real time measurements is performed on the two contact pads with the alligator clips. (c) Sample flowing along the IDE+microfluidic chip during the EIS characterization.

1 and 8 μM actin bundles concentration. At the lower concentration (1 μM) the onset of the semicircle for the kinetic region is observable. Similarly, at the higher concentration of actin bundles (8 μM), a well-defined and larger semicircle is observed representing a higher rate of charge transfer events occurring at the electrode interface. Conversely, for MI buffer no kinetic region is depicted. This result is in agreement with the increased trend in charge transfer resistance, which was found experimentally and modeled for the aforementioned concentrations of actin bundles. This can be explained by the fact that ions at different concentrations have a different free space available to flow easily towards the electrode surfaces upon the application of small AC voltage during EIS.

On the other hand, F-actin diffusion events were not readily detected at concentrations similar to actin bundles (e.g., 1 μM and 8 μM). Bode plots didn't show significance shifting in the formation of the kinetic region of the impedance spectrum as observed on **Fig. S4** in Supplementary Materials. From the baseline given by the KMI buffer (916 Ω), only a 2.7% change (891 Ω) and 3.3% change (885 Ω) of the 1kHz impedance value was observed for the 1 μM and 8 μM F-actin concentration respectively.

F-actin is a charged polyelectrolyte displaying a high charge density where ions condense along the length of the polymer [15], [53], [54], [55]. Molecular modeling has demonstrated that F-actin can sustain a propagation of ionic waves along its length behaving as "electrical wires" due to F-actin's double stranded helical structure [38], [55]. However, the presence of high cation concentration leads to condensation of cations forming a charge density wave bundling F-actin and altering bundle structure and filament helical symmetry [54]. Therefore, minimal alterations to impedance for F-actin are potentially exhibited through sustained propagations of ionic waves along the filament structure, non-condensed filaments that would display minimal alterations to structure and helical twist. In addition, charge transfer phenomena remained the same for this case suggesting that the IDEs are not sensitive enough to capture differences in F-actin concentrations.

It is evident that the microscale-IDE developed in this work was insufficient to get significant F-actin protein coverage onto the electrodes. This affected the sensitivity of the device for in-line impedance measurements. Nanoscale-IDEs might overcome this issue providing a better interfacing area for the protein at that state, and ultimately producing a measurable impedance response at different concentrations of F-actin.

Further the Nyquist plots of the actin filaments and the control buffer were similar and the extracted initial value on the real component of impedance for the buffer and the two concentrations was approximately 12 kΩ for all conditions. Charge transfer phenomena remained the same for this case suggesting possibly that the IDEs are not sensitive enough to capture differences in F-actin concentrations. The reason for this phenomenon is currently being studied.

C. Modeling

1) Electrical Model: Extraction of parameters in the equivalent electrical circuit for actin protein in both states (bundles and filaments) are presented in **Table II**. A comparison between the experimental results, theoretical calculations, and the fitted data using an impedance model was evaluated. Significant variations in the electrical parameters R_{CT}, W, and CPE (Q and α) for actin bundles at different concentrations is observed. Circuit representation is shown in **Fig. 6a** and its impedance equation is provided as [56]:

$$Z = R_S + \frac{R_{CT} + Z_W}{1 + (j\omega)^{\alpha}\, Q(R_{CT} + Z_W)} \tag{1}$$

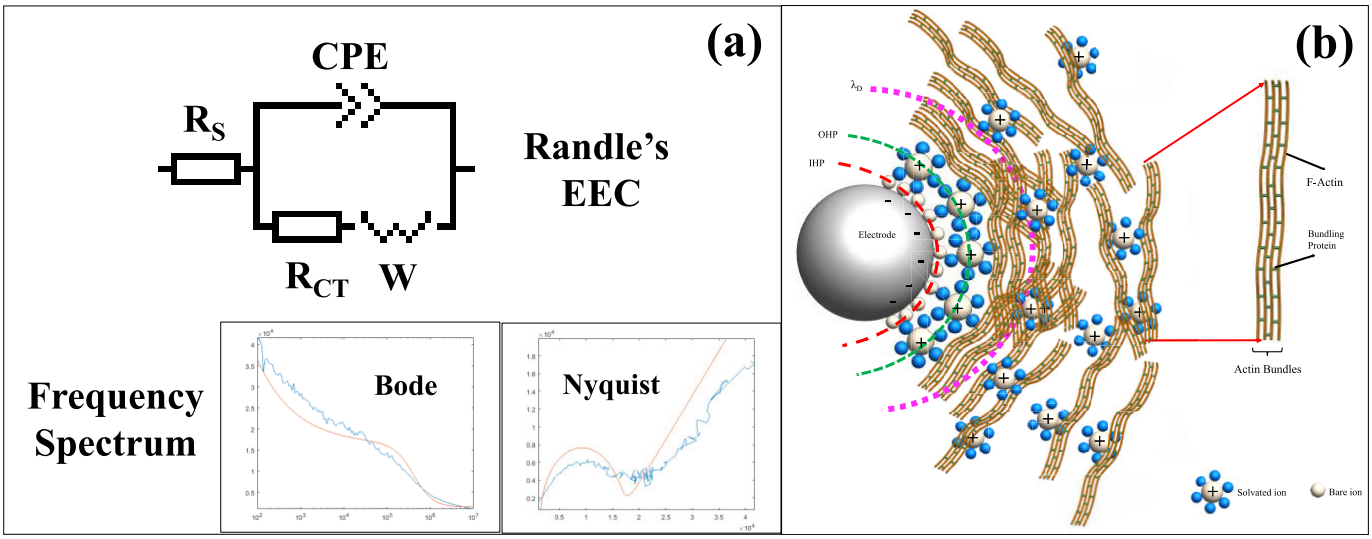

Fig. 6. Electrical modeling and double-layer structure of the interface. (a) Randle's based electrical equivalent circuit (EEC) displaying the solution resistance (R_S), kinetic components such as constant phase element (CPE) and charge transfer resistance (R_{CT}), and the Warburg diffusion element (W). Two frequency spectrum responses (Bode and Nyquist) are depicted to showcase the impedance analysis from the experimental data and modeling approach based on impedance analysis techniques. (b) Visual model of the electrode-solution interface and its double layer capacitance region (drawing not to scale nor actual representation of electrode shape, it is intended to illustrate concepts within the electrochemical cell). Specifically absorbed bare ions near the electrode surface represent the first layer with limits on the Inner Helmholtz Plane (IHP). Nonspecifically absorbed ions referred here as solvated ions create a locus in an extended region with its limit being the Outer Helmholtz Plane (OHP). From this locust to the bulk of solution, Actin bundles protein is found forming thus the second layer or diffusion region. From the OHP to the Debye length (λ_D), there is an exponential decay in the electric potential given by the species concentration and dielectric properties on the sample.

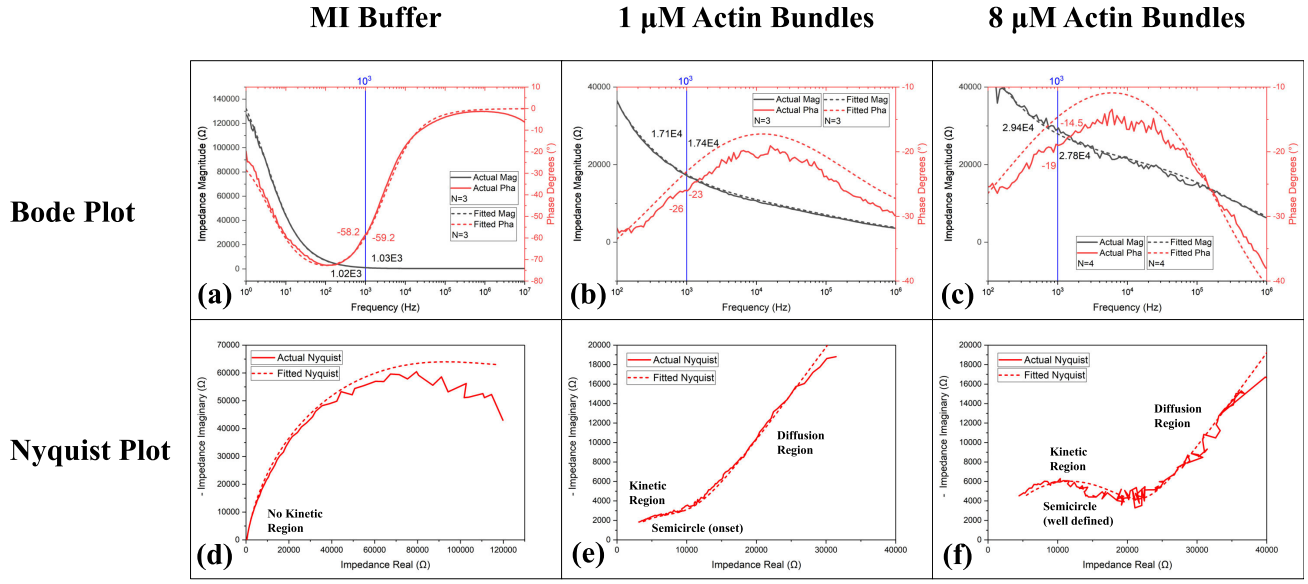

Fig. 7. Electrochemical impedance measurements for actin bundles protein. (a-c) Bode plots from 1 Hz to 10 MHz for the buffer (reference), and 1 μM and 8 μM actin bundle concentration. Impedance magnitude is evaluated at the specific biological frequency of 1 KHz depicting an increased trend upon concentration increase. (d-e) Similarly, Nyquist plot is generated to evidence charge-transfer and species diffusion phenomena upon injection of actin bundles into the microfluidic chip. At 8 μM concentration a clear semicircle on the kinetic region is observed given by the protein film formation. Dotted lines in all the plots is the spectrum given by the EEC model found in each case.

where Warburg (W) and Constant Phase Element (CPE) impedances are defined as [49], [57], [58]:

$$Z_W = \frac{W}{\sqrt{f}} \tag{2}$$

$$Z_{CPE} = \frac{1}{Q(j\omega)^{\alpha}} \tag{3}$$

Here W is the diffusion coefficient, f is frequency in Hertz, and Q is representing an interfacial charging between the surface and the electroactive species. Q is directly proportional to the active area. Constant values of α range from 0 to 1 depending on the tendency of the element to be more resistive (values near to 0) or capacitive (values near to 1).

A previous work of our group showcased how this element might be flexible enough to be used as a substitute for a diffusion element such as the Warburg element in the analysis of 3D microelectrodes [59].

TABLE II
EXTRACTED PARAMETERS FROM THE FITTED ELECTRICAL IMPEDANCE MODEL FOR THE BUFFER, 1μm AND 8μm CONCENTRATION OF ACTIN PROTEIN

Actin State	R_S (Ω)	R_{CT} (Ω)	W ($\Omega.s^{-0.5}$)	Q ($\Omega^{-1}.m^{-2}.s^{\alpha}$)	α	Z_{EXP} [a] (Ω)	Z_{MOD} [b] (Ω)	Z_{THE} [c] (Ω)
Buffer								
Bundles	339	1.33E5	6.62E4	5.37E-7	0.87	1.02E3	1.03E3	1.04E3
Filament	156	1.58E5	34000	5.00E-7	0.88	916	925	NA
1 µM								
Bundles	339	12.28E3	5.61E5	2.13E-7	0.44	1.71E4	1.74E4	2.44E4
Filament	158	1.34E5	39000	6.09E-7	0.86	891	895	NA
8 µM								
Bundles	380	21.22E3	5.12E5	5.79E-9	0.63	2.94E4	2.78E4	2.92E4
Filament	154	1.28E5	37000	6.30E-7	0.85	885	888	NA

[a, b, c] Impedance magnitude at 1 kHz frequency.

According to the results obtained in this modeling, CPE impedance behavior increases upon addition of actin bundles at 1 μM and 8 μM concentrations, influencing mass transport, and decreasing active area which is proportional to the parameter Q. Q value started at 5.37E-7 for the buffer, and ended up two orders of magnitude lower at 5.79E-9 $\Omega^{-1}.m^{-2}.s^{\alpha}$. This is in agreement with the increase in the total impedance value, which is being driven by a charge-transfer resistive behavior of the electrochemical cell. The proof for this interfacial behavior lies in the decreasing tendency in the phase angle from $-58°$ for the buffer up to $-19°$ for the highest concentration of actin bundles observed in the Bode plots of **Fig. 7**.

A theoretical calculation for the interface impedance (Z_I) was performed using electrical impedance concepts at a specific biological frequency. Derivation of Z_I is obtained from equation (1), input parameters are extracted from the EISSA fitting process and the actual actin bundles concentrations that were obtained experimentally (e.g., 1 μM and 8 μM). Thus, interfacial impedance was determined in three different ways: from theory (Z_{THE}), modeling (Z_{MOD}), and experimentally (Z_{EXP}). A one-to-one comparison of this modeling to its experimental value (Z_{EXP}) at 1 kHz frequency as presented in **Table II** for actin bundles.

Derived from equation (2), Warburg impedance results were computed at 2 kΩ, 17.7 kΩ, and 16.2 kΩ for MI buffer, 1 μM, and 8 μM actin bundles concentrations respectively. Following the same sampling order, and using the Warburg impedance for calculations, theoretical interface impedance (Z_{THE}) was computed as 1.04 kΩ, 2.44 kΩ, and 2.92 kΩ. Those Z_{THE} values are in great correlation with the Z_{EXP} experimental data (1.02 kΩ, 1.71 kΩ, and 2.94 kΩ for buffer, 1 μM, and 8 μM concentrations respectively), preserving the same order of magnitude, and low deviation at increased concentration. There is a difference between Z_{MOD} and Z_{THE} for the 1 μM bundle concentration case (17.4 kΩ vs 24.4 kΩ). It is believed this is due to inherent variability during the actin bundle preparation. Purification, polymerization of actin filaments and subsequent aggregation of these into bundles for low concentrations is quite sensitive to extraneous factors such as precise delivery of reagents (volume & concentration), temperature, pH, reaction time, and crowding agents. Z_{MOD} is fitted from experimental data with numerical methods by running 300 iterations of the Powell minimization algorithm for amplitude as weight function [60]. Z_{THE} uses exact values of the concentration parameters. The highest concentration represented the lowest deviation (0.6 % error) from experimental data at 1 kHz.

2) Interfacial Model: Charge transfer phenomena between the metallized electrode and the solution containing the actin bundles was studied by its capacitive effects and potential decay. Debye length, diffuse layer capacitance, and related parameters are calculated from the model described below.

As depicted schematically in **Fig. 6b**, interface between the electrode surface and solution/sample within the cell might be represented physically by a double-layer region containing two specific loci known as Helmholtz planes (inner: IHP, and outer: OHP), and one varying distance representing the diffusion layer. This distance is referred to as the Debye length (λ_D). IHP, OHP, and λ_D along the dielectric constants of the media/actin-species are used to calculate the interfacial capacitance (C_I) combining the linear potential drop within the Helmholtz region, and the exponential drop beyond the OHP.

Double-layer capacitance model proposed by Stern [61] was used to analyze capacitive effects on this interface and the exponential decay on the electric potential. This model proposes that the interface capacitance (C_I) is driven by the combination in series of the Helmholtz capacitance (C_H), and the Gouy-Chapman capacitance (C_G). This way, the capacity of the system takes into consideration the ionic cloud behavior under applied potential. Depending on this potential, and the ion concentration, which is modulated by the acting bundling process, a shift in the Debye length is expected. Thus, the rectification made by Stern to the Gouy-Chapman model suggests this definition for the interfacial capacitance in F/m^2:

$$\frac{1}{C_I} = \frac{1}{C_H} + \frac{1}{C_G} \tag{4}$$

In order to calculate C_H, Inner Helmholtz Plane (IHP) is determined by the size of the specifically absorbed bare ions on the electrode surface. Actin bundles solution is composed of divalent cations Mg^{2+} and sizes for bare and solvated states which are approximately 0.72 and 4.28 Angstrom (Å) respectively [50]. Using the former parameters, the Helmholtz capacitance (C_H) in F/m^2 can be derived from Borkholder [49] as:

$$C_H = \frac{\varepsilon_o + \varepsilon_r}{d_{OHP}} \tag{5}$$

where ε_o is the permittivity in vacuum (8.854×10^{-12} F/m), d_{OHP} is the distance from the electrode surface to the Outer Helmholtz Plane (OHP) in Å ($0.72 + 4.28 = 5$ Å), and ε_r is the solution/sample dielectric constant. Two values (e.g. 5 and 78) for the dielectric constant (ε_r) of actin protein solution referenced from the work of Hunley [16] were used in this research. For the reference buffer saline, the value used for the dielectric constant was 80, similar to water-based medium experiments [62] due to negligible change in this property for these solutions [63].

Determination of C_G requires the Debye length as defined by the following equations [48], [49], [61]:

$$C_G = \frac{\varepsilon_r \varepsilon_o}{\lambda_D} \cosh\left(\frac{zV_o}{2V_t}\right) \tag{6}$$

$$\lambda_D = \sqrt{\frac{\varepsilon_r \varepsilon_o V_t}{2n^o z^2 q}} \tag{7}$$

With V_o being the electrical potential applied to the system (50 mV) emanating from the electrochemical instrumentation, and V_t is the thermal voltage at room temperature given by kT/q (~26 mV). The additional involved variables are elementary charge (q:1.602×10^{-19}C), valence of species (z), and ion concentration (n^o, *in ions/m*^{3}).

Debye length of a buffer solution (no calcium, no magnesium mix) was calculated taking into consideration NaCl species alone, with a concentration of 138 mM, and producing a $\lambda_D = 8$ Å. With respect to the actin bundles at 1 μM and 8 μM concentrations, Mg^{2+} species were considered as the divalent cation required for bundles formation.

Reduction in the Debye length by approximately threefold was calculated upon an increase in actin bundles concentration. Values calculated represented a reduction from 386 to 136 Å for $\varepsilon_r = 5$, and from 1526 to 539 Å for $\varepsilon_r = 78$. This finding is in agreement with Kovacs [48], where at increased concentration of ionic species, the space charge region becomes more compact, thus increasing the magnitude of the interface capacitance. This parameter increased from 0.0038($\varepsilon_r = 5$) to 0.0101($\varepsilon_r = 78$) F/m^2, and from 0.0156($\varepsilon_r = 5$) to 0.0433($\varepsilon_r = 78$) F/m^2 for 1 μM and 8 μM concentrations respectively. There is an evident increasing trend in the value of interface capacitance at increased concentrations of actin bundles as measured by the biosensor.

As far as our knowledge goes, these values are being presented for the first time and building on this work in future studies could ascertain valuable information about this vital protein including interpretation of physiological intracellular states and events such as cytoplasm stiffening, confinement, and induction of molecular crowding, all measured *in vitro*. Complementary studies developed by the Marucho's research group have provided computational characterization of F-actin as polyelectrolyte from molecular structures and finite element modeling [64]. This characterization elucidated the electrical behavior of actin filaments, which is dependent on surface charge density along its irregular structure and surrounding environment. Our future research efforts are aimed to develop a new set of biosensors with increased sensitivity and affinity to actin-F fabricating nano-scale electrodes, to later contrast new findings with computational modeling. The summary of all the calculations for the double-layer structure, and electrode processes in actin bundles are presented in **Table III**.

TABLE III

DEBYE LENGTH (λ_D), INTERFACE CAPACITANCE, AND MODELING PARAMETERS FOR BUFFER SALINE, 1μm AND 8μm CONCENTRATION OF ACTIN BUNDLES PROTEIN

ε_r	Mg^{2+} bare (Å)	Mg^{2+} hydrated (Å)	λ_D (Å)	C_H [a] (F/m^2)	C_G [b] (F/m^2)	C_I [c] (F/m^2)
Buffer						
80	NA	NA	8	1.40	1.33	0.68
1 μM						
5 [d]	0.72	4.28	386	0.09	0.004	0.0038
78 [e]	0.72	4.28	1526	1.38	0.016	0.0156
8 μM						
5 [d]	0.72	4.28	136	0.09	0.011	0.0101
78 [e]	0.72	4.28	539	1.38	0.045	0.0433

[a] Helmholtz capacitance. [b] Gouy-Chapman capacitance. [c] Interface capacitance. Permittivity of the actin protein solution in the [d] condensed, and [e] diffuse layers respectively.

IV. CONCLUSION

A microfluidic biosensor for the *in vitro* detection and flow control of actin filaments and bundles was successfully microfabricated and packaged with demonstrated sensitivity to actin bundles. Integration of laser micromachining techniques such as ablation and scribing along with soft lithography to fabricate the microfluidic biosensor allowed to record impedance values at the critical 1 kHz frequency of 17 kΩ increasing to 30 kΩ upon injection of actin bundles that correlate to protein concentration levels from 1 μM to 8 μM respectively.

Au IDE microelectrodes and PDMS microchannel integration made possible for rapid flow control of actin protein, and real time recording of electrical activity through EIS measurements. Electrical model based on Randles' equivalent circuit of the biosensor was developed from the interface phenomena, providing insights on actin kinetics and electrode materials. Additional efforts in that direction are expected to make possible detection and quantification of actin filaments with nanofluidic channels.

Precise representation of the electrical behavior of the biosensor can be extracted by the parameters from EISSA model along with fitted curves in close proximity to the

experimental results. Physical analysis such as the effect of increased impedance upon injection of actin bundles protein at higher concentrations is derived from values of total impedance, phase angle, and CPE sub parameters. It was found that for 8 μM bundles concentration the interface impedance provided accurate values when comparing theoretical and modeling approaches to the experimental data. The lowest variation for the data in these approaches was 0.6%.

Understanding interface capacitance behavior at different concentrations and dielectric constants is important to identify differences of the electrochemical system when not only electrical forces are acting on the solvated Mg^{2+} ions, but also thermal forces on the nonspecifically absorbed actin bundles in solution. At increased actin bundles concentration, interfacial capacitance increased due to the reduction of the Debye length, which is explained by the low diffusion within the electrolyte. On average, an increase of 272% was obtained for C_I when concentration was increased from 1 μM to 8 μM.

This study reports for the first time to our knowledge that actin bundles concentration can be characterized by electrochemical impedance spectroscopy, and interfacial capacitance analysis integrating microfluidics, and IDE into a single device. This opens new methods of non-invasive analysis of human bioproteins and their implications to disease states among other fundamental studies.

APPENDICES

Appendix A. Supplementary information.

ACKNOWLEDGMENT

The authors would like to thank Materials Characterization Facility (AMPAC) and NanoScience Technology Center, University of Central Florida, for facilitating the use of the tools needed for fabrication and characterization of the device.

REFERENCES

[1] B. T. Schaar and S. K. McConnell, "Cytoskeletal coordination during neuronal migration," *Proc. Nat. Acad. Sci. USA*, vol. 102, no. 38, pp. 13652–13657, Sep. 2005, doi: 10.1073/pnas.0506008102.

[2] T. D. Pollard and J. A. Cooper, "Actin, a central player in cell shape and movement," *Science*, vol. 326, no. 5957, pp. 1208–1212, Nov. 2009, doi: 10.1126/science.1175862.

[3] G. M. Cooper, *The Cell: A Molecular Approach*, 2nd ed. Sunderland, MA, USA: Sinauer Associates, 2000, ch. 2.

[4] J. X. Tang and P. A. Janmey, "The polyelectrolyte nature of F-actin and the mechanism of actin bundle formation," *J. Biol. Chem.*, vol. 271, no. 15, pp. 8556–8563, Apr. 1996, doi: 10.1074/jbc.271.15.8556.

[5] J. Park, M. Lee, B. Lee, N. Castaneda, L. Tetard, and E. H. Kang, "Crowding tunes the organization and mechanics of actin bundles formed by crosslinking proteins," *FEBS Lett.*, vol. 595, no. 1, pp. 26–40, Jan. 2021, doi: 10.1002/1873-3468.13949.

[6] A. P. Minton, "Implications of macromolecular crowding for protein assembly," *Current Opinion Structural Biol.*, vol. 10, no. 1, pp. 34–39, Feb. 2000, doi: 10.1016/s0959-440x(99)00045-7.

[7] I. Kuznetsova, K. Turoverov, and V. Uversky, "What macromolecular crowding can do to a protein," *Int. J. Mol. Sci.*, vol. 15, no. 12, pp. 23090–23140, Dec. 2014, doi: 10.3390/ijms151223090.

[8] N. Castaneda, C. Feuillie, M. Molinari, and E. H. Kang, "Actin bundle nanomechanics and organization are modulated by macromolecular crowding and electrostatic interactions," *Frontiers Mol. Biosciences*, vol. 8, Nov. 2021, Art. no. 760950, doi: 10.3389/fmolb.2021.760950.

[9] J. X. Tang, T. Ito, T. Tao, P. Traub, and P. A. Janmey, "Opposite effects of electrostatics and steric exclusion on bundle formation by F-actin and other filamentous polyelectrolytes," *Biochemistry*, vol. 36, no. 41, pp. 12600–12607, Oct. 1997, doi: 10.1021/bi9711386.

[10] J. Schnauß, T. Händler, and J. Käs, "Semiflexible biopolymers in bundled arrangements," *Polymers*, vol. 8, no. 8, p. 274, Jul. 2016, doi: 10.3390/polym8080274.

[11] N. Castaneda, J. Park, and E. H. Kang, "Regulation of actin bundle mechanics and structure by intracellular environmental factors," *Frontiers Phys.*, vol. 9, pp. 1–7, May 2021, doi: 10.3389/fphy.2021.675885.

[12] H. Ennomani et al., "Architecture and connectivity govern actin network contractility," *Current Biol.*, vol. 26, no. 5, pp. 616–626, Mar. 2016, doi: 10.1016/j.cub.2015.12.069.

[13] N. Castaneda et al., "Cations modulate actin bundle mechanics, assembly dynamics, and structure," *J. Phys. Chem. B*, vol. 122, no. 14, pp. 3826–3835, Apr. 2018, doi: 10.1021/acs.jpcb.8b00663.

[14] L. Blanchoin, R. Boujemaa-Paterski, C. Sykes, and J. Plastino, "Actin dynamics, architecture, and mechanics in cell motility," *Physiological Rev.*, vol. 94, no. 1, pp. 235–263, Jan. 2014, doi: 10.1152/physrev.00018.2013.

[15] E. C. Lin and H. F. Cantiello, "A novel method to study the electrodynamic behavior of actin filaments. Evidence for cable-like properties of actin," *Biophysical J.*, vol. 65, no. 4, pp. 1371–1378, Oct. 1993, doi: 10.1016/s0006-3495(93)81188-3.

[16] C. Hunley and M. Marucho, "Electrical propagation of condensed and diffuse ions along actin filaments," *J. Comput. Neurosci.*, vol. 50, no. 1, pp. 91–107, Feb. 2022, doi: 10.1007/s10827-021-00795-4.

[17] Q. Chen, Z. He, F. Mao, H. Pei, H. Cao, and X. Liu, "Diagnostic technologies for COVID-19: A review," *RSC Adv.*, vol. 10, no. 58, pp. 35257–35264, 2020, doi: 10.1039/d0ra06445a.

[18] J. M. Castro, F. Sommerhage, S. Piranej, D. DeRoo, K. Salaita, and S. Rajaraman, "Multiplexing and increasing the throughput of 'Rolosense Assay' utilizing cost-effective WiFi imaging and disposable microfluidics chips for SARS-COV-2 detection," presented at the *Proc. Hilton Head Workshop Solid-State Sensors, Actuators Microsystems Hilton Head*, 2022, pp. 1–15.

[19] S. H. S. Tali et al., "Tools and techniques for severe acute respiratory syndrome coronavirus 2 (SARS-CoV-2)/COVID-19 detection," *Clin. Microbiology Rev.*, vol. 34, no. 3, Jun. 2021, Art. no. e00228, doi: 10.1128/cmr.00228-20.

[20] J. M. Castro, F. Sommerhage, R. Khanna, A. Childs, D. DeRoo, and S. Rajaraman, "High-throughput microbead assay system with a portable, cost-effective Wi-Fi imaging module, and disposable multilayered microfluidic cartridges for virus and microparticle detection, and tracking," *Biomed. Microdevices*, vol. 25, no. 3, p. 21, Sep. 2023, doi: 10.1007/s10544-023-00661-3.

[21] C. M. Didier, A. Kundu, D. DeRoo, and S. Rajaraman, "Development of in vitro 2D and 3D microelectrode arrays and their role in advancing biomedical research," *J. Micromech. Microeng.*, vol. 30, no. 10, Oct. 2020, Art. no. 103001, doi: 10.1088/1361-6439/ab8e91.

[22] J. S. Choi, H. J. Lee, S. Rajaraman, and D.-H. Kim, "Recent advances in three-dimensional microelectrode array technologies for in vitro and in vivo cardiac and neuronal interfaces," *Biosensors Bioelectron.*, vol. 171, Jan. 2021, Art. no. 112687, doi: 10.1016/j.bios.2020.112687.

[23] J. Manrique Castro and S. Rajaraman, "Experimental and modeling based investigations of process parameters on a novel, 3D printed and self-insulated 24-well, high-throughput 3D microelectrode array device for biological applications," *J. Microelectromech. Syst.*, vol. 31, no. 3, pp. 358–371, Jun. 2022, doi: 10.1109/JMEMS.2022.3160663.

[24] A. Kundu, T. Ausaf, P. Rajasekaran, and S. Rajaraman, "Multimodal microfluidic biosensor with interdigitated electrodes (IDE) and microelectrode array (MEA) for bacterial detection and identification," in *Proc. 20th Int. Conf. Solid-State Sensors, Actuat. Microsystems Eurosensors XXXIII (TRANSDUCERS EUROSENSORS XXXIII)*, Jun. 2019, pp. 1199–1202, doi: 10.1109/TRANSDUCERS.2019.8808696.

[25] H.-S. Shin, V. Gedi, J.-K. Kim, and D.-K. Lee, "Detection of gram-negative bacterial outer membrane vesicles using DNA aptamers," *Sci. Rep.*, vol. 9, no. 1, p. 13167, Sep. 2019, doi: 10.1038/s41598-019-49755-0.

[26] K. Tasnim and J. Liu, "Emerging bioelectronics for brain organoid electrophysiology," *J. Mol. Biol.*, vol. 434, no. 3, Feb. 2022, Art. no. 167165, doi: 10.1016/j.jmb.2021.167165.

[27] C. Hart, A. Kundu, K. Kumar, S. Varma, J. Thomas, and S. Rajaraman, "Rapid nanofabrication of nanostructured interdigitated electrodes (nIDEs) for long-term in vitro analysis of human induced pluripotent stem cell differentiated cardiomyocytes," *Biosensors*, vol. 8, no. 4, p. 88, Oct. 2018, doi: 10.3390/bios8040088.

[28] B. Carnero, C. Bao-Varela, A. I. Gómez-Varela, E. Álvarez, and M. T. Flores-Arias, "Microfluidic devices manufacturing with a stereolithographic printer for biological applications," *Mater. Sci. Eng., C*, vol. 129, Oct. 2021, Art. no. 112388, doi: 10.1016/j.msec.2021.112388.

[29] J. Y. Yoon, *Introduction To Biosensors: From Electric Circuits To Immunosensors*. Berlin, Germany: Springer, 2016.

[30] T. M. Adams and R. A. Layton, *Introductory MEMS : Fabrication and Applications*, 1st ed. Boston, MA, USA: Springer, 2010.

[31] G. T. A. Kovacs, *Micromachined Transducers Sourcebook*. New York, NY, USA: McGraw-Hill, 1998.

[32] J. W. Judy, "Microelectromechanical systems (MEMS): Fabrication, design and applications," *Smart Mater. Struct.*, vol. 10, no. 6, pp. 1115–1134, Dec. 2001, doi: 10.1088/0964-1726/10/6/301.

[33] S. Cosnier, *Electrochemical Biosensors* (Pan Stanford Series on the High-Tech of Biotechnology). Singapore: Pan Stanford, 2013.

[34] C. Hart, K. S. Kumar, J. Li, J. Thomas, and S. Rajaraman, "Investigation of the enhanced sensitivity of interdigitated electrodes for cellular biosensing with geometric, nanostructured surface area, and surface plasmon resonance modes," *J. Microelectromech. Syst.*, vol. 29, no. 5, pp. 1109–1111, Oct. 2020, doi: 10.1109/JMEMS.2020.3012277.

[35] H. Wioland, E. Suzuki, L. Cao, G. Romet-Lemonne, and A. Jegou, "The advantages of microfluidics to study actin biochemistry and biomechanics," *J. Muscle Res. Cell Motility*, vol. 41, no. 1, pp. 175–188, Mar. 2020, doi: 10.1007/s10974-019-09564-4.

[36] M.-F. Carlier, G. Romet-Lemonne, and A. Jégou, "Chapter one—Actin filament dynamics using microfluidics," in *Methods in Enzymology*, vol. 540, R. D. Vale, Ed., New York, NY, USA: Academic Press, 2014, pp. 3–17.

[37] M. X. Yang, X. Hu, D. Akin, A. Poon, and H.-S.-P. Wong, "Intracellular detection and communication of a wireless chip in cell," *Sci. Rep.*, vol. 11, no. 1, p. 5967, Mar. 2021, doi: 10.1038/s41598-021-85268-5.

[38] C. Hunley, D. Uribe, and M. Marucho, "A multi-scale approach to describe electrical impulses propagating along actin filaments in both intracellular andin vitroconditions," *RSC Adv.*, vol. 8, no. 22, pp. 12017–12028, 2018, doi: 10.1039/c7ra12799e.

[39] S. Rajan, D. S. Kudryashov, and E. Reisler, "Actin bundles dynamics and architecture," *Biomolecules*, vol. 13, no. 3, p. 450, Feb. 2023, doi: 10.3390/biom13030450.

[40] N. Adly et al., "Printed microelectrode arrays on soft materials: From PDMS to hydrogels," *NPJ Flexible Electron.*, vol. 2, no. 1, p. 15, May 2018, doi: 10.1038/s41528-018-0027-z.

[41] C. Hart and S. Rajaraman, "Low-power, multimodal laser micromachining of materials for applications in sub-5 μm shadow masks and sub-10 μm interdigitated electrodes (IDEs) fabrication," *Micromachines*, vol. 11, no. 2, p. 178, Feb. 2020, doi: 10.3390/mi11020178.

[42] A. Butkutė et al., "Combined femtosecond laser glass microprocessing for liver-on-chip device fabrication," *Materials*, vol. 16, no. 6, p. 2174, Mar. 2023, doi: 10.3390/ma16062174.

[43] L. O'Connell et al., "Rapid fabrication of interdigitated electrodes by laser ablation with application to electrokinetically enhanced surface plasmon resonance imaging," *Opt. Laser Technol.*, vol. 161, Jun. 2023, Art. no. 109167, doi: 10.1016/j.optlastec.2023.109167.

[44] A. Manzoli et al., "Femtosecond laser ablation of gold interdigitated electrodes for electronic tongues," *Opt. Laser Technol.*, vol. 69, pp. 148–153, Jun. 2015, doi: 10.1016/j.optlastec.2014.12.026.

[45] N. Azim, N. Castaneda, A. Diaz, H. Kang, and S. Rajaraman, "Multimodal microelectrode arrays for the investigation of protein actin's electro-mechanosensing mechanisms toward neurodegenerative disease models on a chip," in *Proc. Solid-State, Actuators, Microsystems Workshop*, 2018, pp. 253–256.

[46] H. Kang et al., "Identification of cation-binding sites on actin that drive polymerization and modulate bending stiffness," *Proc. Nat. Acad. Sci. USA*, vol. 109, no. 42, pp. 16923–16927, Oct. 2012, doi: 10.1073/pnas.1211078109.

[47] A. Bondarenko and G. Ragoisha, "Inverse problem in potentiodynamic electrochemical impedance," in *Progress in Chemometrics Research*, A. L. Pomerantsev, Ed., New York, NY, USA: Nova Science Publishers, 2005, pp. 89–102.

[48] G. Kovacs, "Introduction to the theory, design, and modeling of thin-film microelectrodes for neural interfaces," in *Enabling Technologies for Cultured Neural Networks*. USA: Academic, 1994.

[49] D. A. Borkholder, *Cell-Based Biosensors Using Microelectrodes*. Stanford, CA, USA: Stanford University, 1999.

[50] C. Zhong, Y. Deng, W. Hu, J. Qiao, L. Zhang, and J. Zhang, "A review of electrolyte materials and compositions for electrochemical supercapacitors," *Chem. Soc. Rev.*, vol. 44, no. 21, pp. 7484–7539, 2015, doi: 10.1039/c5cs00303b.

[51] S. W. Lee and S. S. Lee, "Shrinkage ratio of PDMS and its alignment method for the wafer level process," *Microsyst. Technol.*, vol. 14, no. 2, pp. 205–208, Oct. 2007, doi: 10.1007/s00542-007-0417-y.

[52] *QuickLaze-50ST Operator's Manual*, NWR Inc, Fremont, CA, USA, 2005.

[53] G. S. Manning, "Counterion binding in polyelectrolyte theory," *Accounts Chem. Res.*, vol. 12, no. 12, pp. 443–449, Dec. 1979, doi: 10.1021/ar50144a004.

[54] T. E. Angelini, H. Liang, W. Wriggers, and G. C. L. Wong, "Like-charge attraction between polyelectrolytes induced by counterion charge density waves," *Proc. Nat. Acad. Sci. USA*, vol. 100, no. 15, pp. 8634–8637, Jul. 2003, doi: 10.1073/pnas.1533355100.

[55] J. A. Tuszyński, S. Portet, J. M. Dixon, C. Luxford, and H. F. Cantiello, "Ionic wave propagation along actin filaments," *Biophysical J.*, vol. 86, no. 4, pp. 1890–1903, Apr. 2004, doi: 10.1016/s0006-3495(04)74255-1.

[56] S. Wang, J. Zhang, O. Gharbi, V. Vivier, M. Gao, and M. E. Orazem, "Electrochemical impedance spectroscopy," *Nature Rev. Methods Primers*, vol. 1, no. 1, p. 41, Jun. 2021, doi: 10.1038/s43586-021-00039-w.

[57] V. F. Lvovich, *Equivalent-Circuit Elements and Modeling of the Impedance Phenomenon*. USA: Wiley, Jul. 2012, pp. 37–47, doi: 10.1002/9781118164075.ch3.

[58] J.-B. Jorcin, M. E. Orazem, N. Pébère, and B. Tribollet, "CPE analysis by local electrochemical impedance spectroscopy," *Electrochimica Acta*, vol. 51, nos. 8–9, pp. 1473–1479, Jan. 2006, doi: 10.1016/j.electacta.2005.02.128.

[59] J. Manrique Castro and S. Rajaraman, "Constant phase element (CPE) modeling and analysis of multi-material, micro-bullet shaped, high-throughput 3D microelectrodes for in-vitro electrophysiological applications," in *Proc. Solid-State, Actuat., Microsystems Workshop Tech. Dig.*, Jun. 2022, pp. 407–410.

[60] M. J. D. Powell, "An efficient method for finding the minimum of a function of several variables without calculating derivatives," *Comput. J.*, vol. 7, no. 2, pp. 155–162, Feb. 1964, doi: 10.1093/comjnl/7.2.155.

[61] A. J. Bard and L. R. Faulkner, *Electrochemical Methods: Fundamentals and Applications*, 1st ed. Hoboken, NJ, USA: Wiley, 1980.

[62] S. Flock, R. Labarbe, and C. Houssier, "Dielectric constant and ionic strength effects on DNA precipitation," *Biophysical J.*, vol. 70, no. 3, pp. 1456–1465, Mar. 1996, doi: 10.1016/s0006-3495(96)79705-9.

[63] J. Liang, X. Zhao, D. Kong, Y. Chen, and T. Ueda, "Effect of properties of phosphate buffer saline solutions on vibrational characteristics of a quartz crystal microbalance resonator," *Sensors Mater.*, vol. 30, no. 5, pp. 1115–1121, 2018.

[64] S. Manrique-Bedoya and M. Marucho, "Molecular structure study on the polyelectrolyte properties of actin filaments," *RSC Adv.*, vol. 12, no. 10, pp. 6314–6327, 2022, doi: 10.1039/d1ra09280d.

Jorge Manrique Castro received the B.S. degree in electronics engineering from the National University of Colombia in 2007, the Master in Business Administration degree from the University of Valle in 2018, and the M.S. and Ph.D. degrees in electrical engineering from the University of Central Florida in 2022 and 2023, respectively.

He is currently a Post-Doctoral Scholar with the NanoScience Technology Center, University of Central Florida. Skilled in industrial applications and process automation, he worked in the electronic instrumentation field for more than ten years in technical and managerial roles implementing sensors, transducers, and data acquisition systems from different manufacturers. His professional activities were focused in industrial process control, measurement and monitoring of various variables within the

energy, environmental, and manufacturing fields. He was a Technical Trainer of technicians and engineers and worked for three years in Colombia as a Consultant. After transitioning from the industrial-instrumentation to bio-instrumentation, his scientific research involved the makerspace fabrication, optimization, and modeling of in-vitro platforms allowing intimate interfacing between 3D microfeatures and multisized biological entities with potential use in drug response and electrophysiological studies. He worked in the fabrication of impedimetric biosensors for protein detection using soft-lithography, laser ablation, and metal deposition techniques. Also, he developed multilayered high-throughput microfluidic chips facilitating the running of biological assays for virus detection where micromilling, precise plotter and laser materials cutting, and surface characterization were carried out. The scientific production emanating from his research has resulted in publication of 15 manuscripts (five journal articles and ten conferences papers), one editorial, and three patents. He has been awarded several scholarships, such as the renowned Daniel D. Hammond Engineering Scholarship and the Latin American and Caribbean Scholarship. He is passionate about bioengineering applications demanding microfabrication, sensing, transduction, and modeling. His current research interests are related to designing, testing, optimizing technologies involving microelectrode arrays (MEAs), interdigitated electrodes (IDEs), and micro/nano electromechanical systems (M/NEMS) for real-life applications in biosystems. The development of robust biosensors with novel microstructures through makerspace microfabrication, rapid prototyping, and correlating bioelectronics with materials science to provide solutions in wearable and implantable biomedical systems are his incoming challenges.

Dr. Castro research have been also recognized and awarded in the IEEE MEMS 2022, IEEE MEMS 2023, and MIST 2023 Conferences as Best Paper, an Outstanding Finalist, and a Best Poster, respectively.

Nilab Azim received the B.S. degree in chemistry and in biology from the University of North Florida, Jacksonville, FL, USA, and the Ph.D. degree in chemistry with a focus in materials chemistry from the University of Central Florida, Orlando.

Her previous research focused on fabrication of biosensors, the integration of non-traditional materials with devices, and the study of polymer nanomaterials. Her academic research work resulted in 13 journals and conference proceeding publications, four of which were first-author publications. Previously, she was a Chemical Engineer. She is currently a Principal Investigator and the Project Manager of the NASA's Kennedy Space Center's Exploration Systems & Development Office.

Dr. Azim was selected as a Speaker at the North American Materials Colloquium Series and presented at three national conferences.

Nicholas Castaneda received the B.S. degree in biology from Florida International University, Miami, FL, USA, and the Master of Science degree in nanotechnology and the Ph.D. degree from the University of Central Florida, Orlando.

His previous research focused on the interactions of various environmental factors, including ions and macromolecular crowding with actin filaments and bundles. His academic achievements can be summarized to include five first-author peer-reviewed publications, collaborations on three additional publications and receiving the Chateaubriand Fellowship Award. In addition, he presented at 16 national conferences, of which three were invited talks and five resulted in presentation awards.

Ellen Kang received the B.S. and M.S. degrees in physics from Seoul National University, Seoul, South Korea, and the Ph.D. degree in physics (biophysics) from Brown University, Providence, RI, USA.

She was a Visiting Doctoral Student with the University of Pennsylvania, Philadelphia, PA, USA. She was a Post-Doctoral Research Associate with the Department of Molecular Biophysics and Biochemistry, Yale University, New Haven, CT, USA, prior to joining the University of Central Florida (UCF) in Fall 2015. She is currently an Associate Professor in physics with the NanoScience Technology Center and the Department of Physics, UCF. At UCF, she leads a molecular biophysics research group, with a focus on cytoskeletal protein biomechanics and mechanobiology. Specifically, she and her research team incorporates molecular biophysics and nanoscale tools to identify fundamental mechanisms by which various intracellular and extracellular environments modulate the conformations, mechanics, and mechanosensing of the actin cytoskeleton. Her research projects have been supported by the National Science Foundation, National Institute of Health, and NASA FSRP.

Prof. Kang is a member of the American Physical Society (APS), Biophysical Society (BPS), and Korean-American Scientists and Engineers Association (KSEA). She serves as a Committee Member for BPS, served as a Treasury Secretary for Association of Korean Physicists in America (AKPA) (2021–2023), and was recently elected as the President Elect (2023–2025). She serves as the President for KSEA Central Florida Chapter (2023–2024). She has won the prestigious National Science Foundation CAREER Award.

Swaminathan Rajaraman (Member, IEEE) received the B.S. degree in electronics engineering from Bharathidasan University, Trichy, India, the M.S. degree in electrical engineering from the University of Cincinnati, Cincinnati, OH, USA, and the Ph.D. degree in electrical engineering from Georgia Institute of Technology, Atlanta, GA, USA.

He is currently an Academic and a Successful Entrepreneur. He is also an Associate Professor with the NanoScience Technology Center and the Department of Materials Science and Engineering, University of Central Florida, Orlando, FL, USA. He runs a very interdisciplinary group composed on electrical engineers as a Biomedical Scientists, a Material Scientists, a Mechanical Engineers, and a Chemists. His current research interests include in-vitro and in-vivo microelectrode arrays (MEAs), micro/nanofabrication, micro/nanofabrication on novel, biological substrates, microneedles, agricultural microsystems, microfluidic devices, multimodal cell-based nanosensors, 3D printing, and implantable MEMS devices. Prior to his academic appointment, he has worked in the micro-electro-mechanical systems (MEMS) industry and co-founded Axion BioSystems Inc., Atlanta, GA, USA, a world-leader in high-throughput microelectrode arrays (MEAs) and MEA systems during the Ph.D. work. After 13 years of operation in July 2021, he was successfully acquired by Swedish Private Equity Firm, Summa Equity. In December 2020, he co-founded his second company, Primordia BioSystems Inc., to commercialize concepts from his UCF research group. His work has resulted in approximately 80 peer-reviewed journals and conference papers, 30 patent and patent applications and several products in volume production.

Prof. Rajaraman has been a member of the Editorial Board of *Scientific Reports* (Nature) since 2019. In 2021, he was elected to the Board of Directors of the Transducers Research Foundation. He was the Track Chair of a Bioelectric Sensors Session in IEEE EMBC 2010, the Session Co-Chair at NanoFlorida in 2018 and 2019, and the Session Co-Chair at IEEE MEMS in 2020 and IEEE MEMS in 2021. He has served on the Technical Program Committee (TPC) for the Solid State Sensors, Actuators and Microsystems Workshop (Hilton Head 2014, 2016, and 2022), as the Vice Chair for Commercial Development in Hilton Head MEMS 2020, and the Chair of Commercialization Development in the same meeting for 2022. He is also the Program Chair of the same meeting in 2024. Additionally, he has served on the TPC of IEEE Sensors Conference in 2016 and 2017 and the TPC of IEEE Transducers in 2021 and 2023. In 2023, he additionally serves on the editorial board for IEEE/ASME JOURNAL OF MICRELECTROMECHANICAL SYSTEMS.